SAE INTERNATIONAL

ARTICLE INFO

Article ID: 04-11-01-0001
Published: 16 Feb 2018

doi:10.4271/04-11-01-0001

Investigations on Spark and Corona Ignition of Oxymethylene Ether-1 and Dimethyl Carbonate Blends with Gasoline by High-Speed Evaluation of OH* Chemiluminescence

Thorsten Langhorst, Karlsruhe Institute of Technology (KIT)

Olaf Toedter, Thomas Koch, Benjamin Niethammer, Ulrich Arnold, and Jörg Sauer,
Karlsruhe Institute of Technology (KIT)

Abstract

Bio-fuels of the 2nd generation constitute a key approach to tackle both Greenhouse Gas (GHG) and air quality challenges associated with combustion emissions of the transport sector. Since these fuels are obtained of residual materials of the agricultural industry, well-to-tank CO_2 emissions can be significantly lowered by a closed-cycle of formation and absorption of CO_2. Furthermore, studies of bio-fuels have shown reduced formation of particulate matter on account of the fuels' high oxygen content therefore addressing air quality issues. However, due to the high oxygen content and other physical parameters these fuels are expected to exhibit different ignition behaviour. Moreover, the question is whether there is a positive superimposition of the fuels ignition behaviour with the benefits of an alternative ignition system, such as a corona ignition. To shed light on these questions two oxygenic compounds, oxymethylene ether-1 (OME1) and dimethyl carbonate (DMC) have been studied with respect to OH* emission throughout ignition and onset of flame-front propagation in a combustion chamber with a large optical access via a quartz window. OH* measurements have been recorded via a high-speed optical camera (5 kHz) coupled with 308 nm optical filter and image intensifier. Sealing material swelling tests have yielded a perfluoroelastomer (FFKM 72) as an ideal, cost-efficient material regardless of the applied fuel. Comparative measurements with both ignition systems for combustion of gasoline as well as moderate blend admixtures of OME1 and DMC have demonstrated the superior ignition stability with likewise implications on flame-kernel development for the corona ignition. Furthermore a strong influence of the mode of discharge on OH* formation rates was observed especially for the oxygenic blends. Finally, for admixture variations of both oxygenates, an increased OH* level was shown during discharge thereby proving the hypothesis of a positive superimposition of oxygenic fuel and corona ignition system.

History

Received:	23 Aug 2017
Revised:	06 Oct 2017
Accepted:	20 Oct 2017
e-Available:	01 Mar 2018

Keywords

Oxygenate, NTP, Corona, OH, SI, High-Speed, OME, DMC, Inflammation, PM

Citation

Langhorst, T., Toedter, O., Koch, T., Niethammer, B. et al., "Investigations on Spark and Corona Ignition of Oxymethylene Ether-1 and Dimethyl Carbonate Blends with Gasoline by High-Speed Evaluation of OH* Chemiluminescence," *SAE Int. J. Fuels Lubr.* 11(1):2018, doi:10.4271/04-11-01-0001.

ISSN: 1946-3952
e-ISSN: 1946-3960



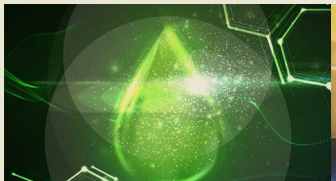

Introduction

Legislation forces a reduction of CO_2 emissions for the road transport sector [1, 2, 3]. Current approaches to meet these requirements comprise reduction of fuel consumption, substitution of liquid fossil fuels by gaseous fossil fuels with more favourable H/C-ratio or usage of synthetic fuels from regenerative resources. Gaseous or liquid synthetic fuels are produced either by electrolysis of water with excess electricity (Power to X, PtX) or by the conversion of biomass (Biomass to Liquid, BtL). Ethanol, as the most relevant bio-fuel, has been market-introduced in various countries, both as an additive in mixtures of up to 10 Vol.-% (Germany, US), 25 Vol.-% (Brasil) and as a major substituent with 85 Vol.-% (US). As a 1st generation bio-fuel, however, the cultivation of biomass for ethanol production competes with conventional food cultivation for arable land and resources such as water and fertiliser [4]. Furthermore, cultivation and production just as well emit CO_2 thereby making it impossible to realise a closed CO_2 cycle [5]. The increased oxygen content of ethanol-gasoline blends reduces the formation of products resulting from incomplete combustion, such as Particulate Matter (PM), due to higher reactivity and altered morphology of the formed particulates [6, 7, 8, 9]. Nevertheless, due to increased heat of vaporisation and reduced energy content, mixture formation has to be well controlled to prevent local fuel-rich areas and increased PM emission hereby [10].

Bio-fuels of the 2nd generation, in contrast, are produced of unspecific organic residuals, thus increasing the utilisation factor of the plant. Such BtL-fuels are obtained by pyrolysis and gasification of biomass to syngas ($CO + H_2$), followed by various subsequent process steps towards a liquid bio-fuel. For example, the Dimethylether to Gasoline (DtG) process is used in the bioliq® pilot plant at KIT (Karlsruhe Institute of Technology), to generate gasoline-range hydrocarbons [11]. Another option to process syngas is to produce oxygenic fuels (oxygenates). In this case, the oxygen of the raw material can partially remain in the product, which allows production with high energetic and atomic efficiency. Oxymethylene ethers (OME_n, $CH_3(OCH_2)_nOCH_3$) [12, 13] are currently investigated to optimise PM emission behaviour of diesel combustion. Several studies [14, 15, 16, 17] have demonstrated significant reductions of PM emissions by admixture of OME1, which can be attributed to its high oxygen content (42.1 wt.-% [12]) and non-existent C-C bonds (acetylene hypothesis [18]).

According to the best of the authors' knowledge, OME1-gasoline blends have not been investigated yet and are tested in this publication for the first time. In addition a second oxygenate, dimethyl carbonate (DMC) is investigated, which can also be sustainably produced via processing of syngas. DMC exhibits a further increased oxygen content (53.3 wt.-%) and high auto-ignition temperature (458 °C [19]), which renders it a suitable fuel for SI combustion. The introduction of the WLTC test-procedure, implemented in Europe by Euro 6d-TEMP in September 2017 [20, 21, 22], exacerbates compliance with particulate emission limits. Additionally, the introduction of the gasoline particulate filter (GPF) [23] adds cost and complexity to the comparatively inexpensive gasoline drivetrain. Thereby, the implementation of oxygenates as an additive to gasoline holds additional appeal.

Challenges in mixture formation, such as increased fuel volumes on account of low fuel energy content (23.3 MJ/kg for OME1 [12]), have to be overcome for an ideal applicability. A possible pathway could be a lean, homogeneous combustion process. In this area, alternative ignition concepts such as a corona-ignition have demonstrated benefits in terms of ignition stability of diluted mixtures [24, 25, 26, 27]. A corona-ignition generates a non-thermal plasma (NTP), i.e. the plasma is not in thermodynamic equilibrium [25] and electron temperatures (hot) differ significantly from those of the ions (cold) within the gas. Large amounts of radicals, such as OH*, O, O_3 are formed by electron impact along the partial discharge's streamers [27, 28] and thus initiate flame kernel development chemically, whereas a spark-plug obtains smaller radical counts by thermal initial radical formation. Hence increased levels of excited hydroxyl radical emission (OH*) have been measured [29] throughout ignition until onset of flame-front propagation, compared to conventional spark-plug ignition. OH*, besides O_3 and O radicals, are known oxidising agents of elemental carbon [30, 31] which in turn represents the major constituent of particulate matter.

Both OME1 and DMC might produce increased levels of OH* because of their high oxygen content, analogous to behaviour reported with ethanol [7, 32]. Hence, the OH* level, as both a tracing element to ignition and flame-front propagation [33, 34, 35] and an indicator to engine-internal PM emission reduction potential, is investigated in this study for combinations of two different ignition systems with various blends of the two aforementioned oxygenates. Ultimately, the goal of the experiments is to identify benefits of the corona-ignition over the spark-plug ignition in terms of stability of ignition and onset of flame-front propagation. Furthermore the interrelation of these properties to the degree of OH* chemiluminescence during both stages of combustion is to be demonstrated. Lastly, potential benefits in these aspects, measured by OH* signal, shall be investigated when blending gasoline with oxygenates OME1 and DMC. The improved understanding of the behaviour of oxygenates during combustion, so that all of their aforementioned benefits may be utilised, is a further step on the way towards de-carbonisation and emission reduction of the transport sector.

Experimental Setup

The experiments have been conducted on a constant-volume combustion chamber (CVCC) which is of square design with a displacement of 686 cm^3. It features a pent-roof cylinder head with centrally mounted ignition system and slightly tilted injector. Optical accessibility is realised by a 50 mm thick, planar quartz glass window whereby combustion can be observed free of optical distortion. To generate turbulence, a plate with three eccentric holes can be shot downwards within the chamber. Initial chamber pressure is restricted

TABLE 1 Operational parameters of the CVCC.

Parameter	Unit	Value
Chamber volume	cm^3	686
Injection pressure	MPa	20
Temperature chamber walls	°C	50
Temperature intake air	°C	130
Pressure chamber	MPa	0.1
Equivalence ratio λ	-	0.73
Corona burst duration	ms	1.4
Corona frequency	MHz	4.560
Spark-plug energy	mJ	90
Turbulence plate 'UP'	ms	0[a]
Turbulence plate 'DOWN'	ms	500[a]
Injection timing	ms	575[a]
Ignition timing (and camera trigger)	ms	2576[a]
LaVISION IRO Gate	ns	40000
LaVISION IRO Gain	%	60
LaVISION HSS6 exposure time	ms	0.2

[a] Given values represent electronic triggering order of devices.

to ambient pressure conditions due to limited quartz glass strength and safety regulations (cf. Table 1). Measurements of ignition delay for iso-Octane [36] have shown reduced delay times towards higher pressures and a shift of the NTC-area (negative temperature coefficient) towards higher temperatures. Since the CVCC is operated at boundary conditions below the NTC-area, i.e. exponential correlation of ignition delay and temperature, the results of this paper can be qualitatively translated towards more realistic operating conditions. Supply of fresh air and discharge of exhaust gases is realised via magnetic valves that are remotely actuated. Fresh air is supplied with 130 °C by a heated line and the CVCC's walls are heated to 50 °C. In Figure 1 a photograph of the CVCC is shown.

Fuel is supplied by a high-pressure common-rail system driven by an electric motor and is injected with a 6-hole Bosch HDEV 5.2 injector. Ignition systems used in this publication are a Bosch Platin spark plug (electrode gap = 0.7 mm) and a Borg-Warner EcoFlash corona ignition system with a single-prong igniter. In Figure 2 the orientation of fuel injector and spark plug within the cylinder head is presented.

The optical high-speed setup consists of a LaVISION HSS6 high-speed camera (5 kHz), UV-sensitive lens, Edmund Scientific bandpass-filter (307 +/– 5 nm) for OH* detection, LaVISION IRO image intensifier and LaVISION DaVis 8.4 software. The recording frequency is a compromise between hard-disk storage volume and optical resolution of the phases of ignition which consist of breakdown, arc mode and glow mode. Each of these phases exhibit different lifetimes which range from 10 ns (breakdown) to several milliseconds (glow mode) [37]. The test-rig is automated by means of a National Instruments CompactRIO system which has an FPGA controller allowing to be parameterised via a National Instruments LabVIEW GUI. The automation controls gas-exchange and triggers injection, ignition and high-speed

FIGURE 1 Photograph of the CVCC.

image acquisition. The automated sequence is schematically presented in Figure 3.

In Table 1 operational parameters of the experimental setup as well as timings for turbulence plate, injection and ignition are summarized.

Fuels

In this publication two alternative oxygenic fuels have been investigated apart from conventional RON95 gasoline. The first fuel is oxymethylene ether-1 (OME1), the second fuel dimethyl carbonate (DMC). Both fuels have been purchased

FIGURE 2 CAD model of CVCC cylinder head in camera perspective with injector (left) and spark plug (right).

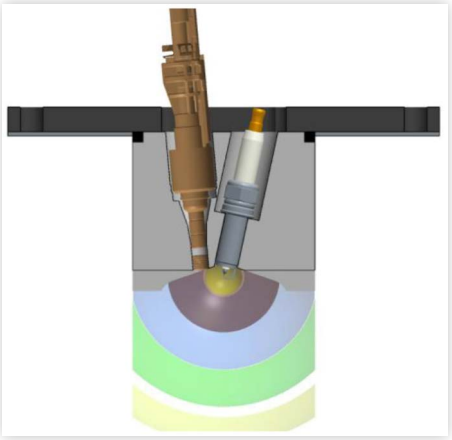

FIGURE 3 Automated experimental sequence of chamber gas exchange, turbulence generation, injection, ignition and optical triggering.

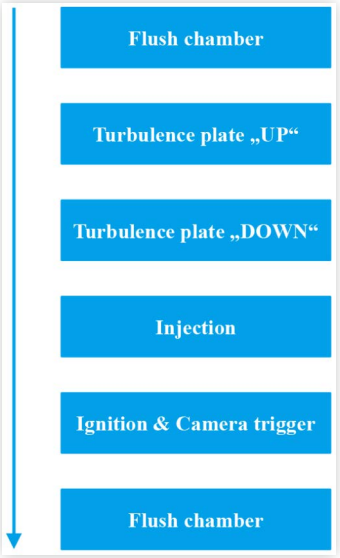

externally. The physical properties of all three pure fuels are summarised in Table 2.

Boiling curves for gasoline and all gasoline-oxygenate blends used in this publication have been measured and are presented in Figure 4. Admixtures of 5 Vol.-% are labelled in grey, admixtures of 10 Vol.-% in green and admixtures of 50 Vol.-% in blue. It can be seen that admixtures of 5 and 10 Vol.-% do not significantly alter the boiling behaviour regardless of the blending component.

In order to test the compatibility of the gasoline-oxygenate blends with the sealing materials in the test-rig, the swelling behaviour of several elastomer sealing rings (purchased by COG, Germany), after being exposed to the blends, was investigated. Best results for all OME1 and DMC blends in terms of low swelling can be achieved with PER G75 LT, which is also referred to as FFKM 72, a cost-efficient perfluoroelastomer. A more detailed description of the experimental procedures can be found in the Appendix.

TABLE 2 Fuel parameters.

Property	Unit	RON95	OME1	DMC
Formula	-	$C_{6.6}H_{13}O_{0.14}$	$C_3H_8O_2$	$C_3H_6O_3$
CAS			109-87-5	616-38-6
O_2 content	wt.-%	0	42.1	53.3
$\Delta H_{vaporisation}$	kJ/kg	420 [38]	375.65 [39]	425.89 [40]
Density	kg/m³	728.4	867	1007
Stoich. ratio	kg/kg	14.31	7.23	4.58
LHV	MJ/kg	42.39	23.30	14.50
RON	-	95.7	28 (CN) [41]	-
MON	-	85.8		
T_B	°C	31-187	42 [12]	90.5 [42]
T_M	°C	N/A	−105.1 [43]	0.5 [43]

FIGURE 4 Boiling curves for gasoline, OME1-blends and DMC-blends.

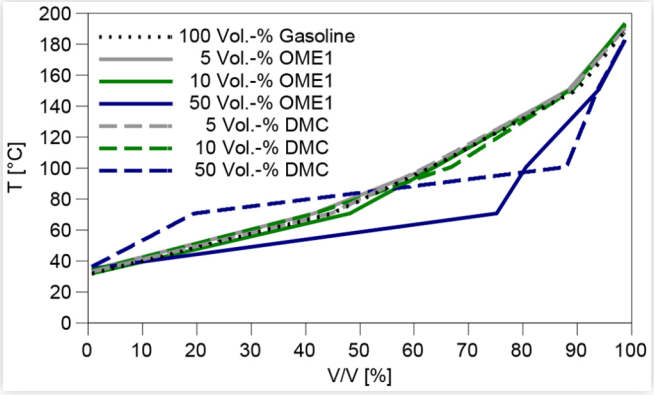

Experimental Results

In this chapter, the experimental results are presented. To ensure reproducibility and to obtain statistical data each experiment was repeated ten times. As for the corona ignition system, only repetitions without electrical breakdown (arc) are considered. In this publication, the term ignition summarises the process steps of electrical breakthrough (or occurrence of NTP), energy-transfer into the gas and formation of intermediate, reactive radicals and, finally, early flame-kernel development.

Robustness of Optical Analysis Tool-Chain

All optical data have been captured and exported to PNG images with LaVISION DaVis 8.4 software. The exported files were then processed via a post-processing routine in MATLAB which has been developed by the authors. The processing steps are as follows:

1. Conversion of RGB image to 8-bit greyscale
2. Determine image noise (individual to each picture)
   a. Extract narrow vertical strip across height of image beyond framed combustion chamber contour
   b. Calculate mean greyscale value for vertical strip
3. Multiply image with black mask with coordinates of combustion chamber contour
4. Binarise image with condition: Image >7 · $mean_{noise}$
5. Filter binarised image with median-filter of 15 × 15 width to reduce salt and pepper effects
6. Perform calculations (Area, statistics, flame-contour, superposition, et cetera)

In order to evaluate robustness of the above described algorithm, a sensitivity study has been performed where various parameters such as vertical strip (position, orientation), threshold factor (here: 7), median filter (position,

FIGURE 5 Raw and binarised images for corona ignition (first two columns) and spark-plug ignition (third and fourth column).

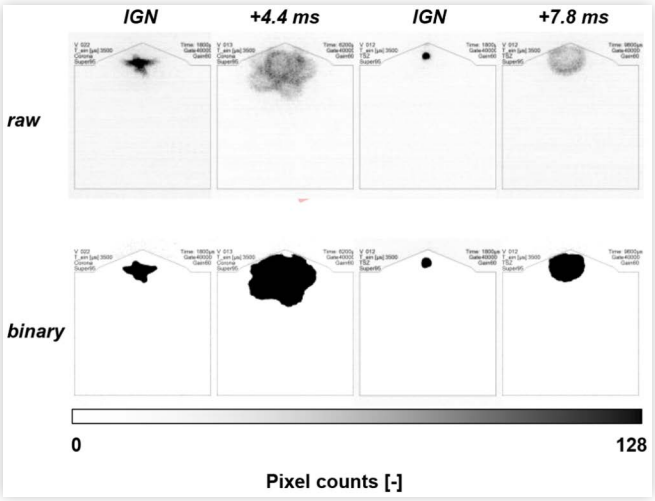

FIGURE 6 OH* signal for both ignition systems with pure gasoline at discrete time steps after ignition.

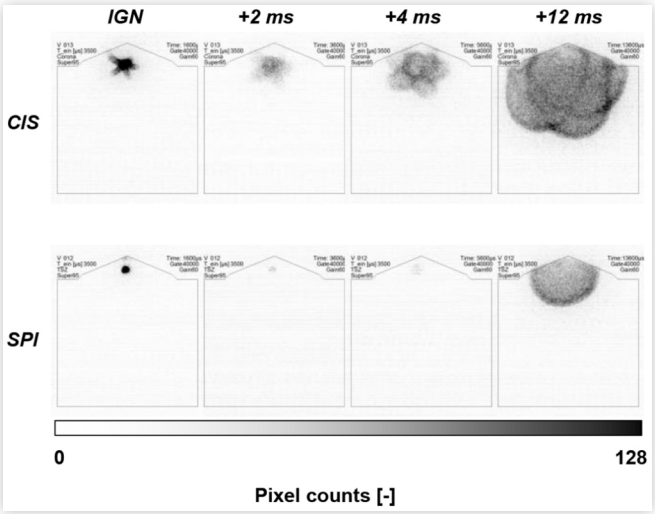

number of applications, filter width) have been varied. Furthermore the algorithm has been tested against the thresholding method by Otsu [44] which has then been applied for noise correction only. All modifications yielded similar binarisation results. A comparison of raw and binarised images for corona ignition (first two columns) and spark-plug ignition (third and fourth column) with the applied algorithm is shown in Figure 5. The pictures have been inverted for better visibility.

Comparison Spark-Plug vs. Corona Ignition System with RON-95 Gasoline

In this sub-chapter an introductory comparison between conventional spark-plug ignition (SPI) and corona ignition system (CIS) for ignition of a stoichiometric gasoline-air mixture is drawn. In Figure 6 the OH* signal of exemplary cycles at point of ignition and several subsequent time-steps are shown for both systems. The pictures have been inverted for better visibility.

First of all at ignition ('IGN') the different volumes of corona with star-like spreading of its streamers and spark can be noted. After that, for the CIS, a monotonous increase of detected OH* follows. Furthermore multiple OH* clouds marked by thick, bright boundaries, which apparently originate from individual streamers, have formed starting at 4 ms. These boundaries are regions of high OH* density and trace the outline of the flame-front [45]. As for the SPI, after the small, roundish OH* signal at ignition, the signal has all but entirely vanished at 2 ms after ignition. It is only after 8 ms that a substantially smaller OH* cloud than that of the CIS is evident. No multiple boundaries can be noted. The thermodynamic effects of the above discussed differences, such as higher initially affected volume, multiple flame-kernels and reduced ignition delay have been investigated by several authors [24, 25, 26, 27]. Except for a publication by Toedter et al. [29] the authors are unaware of other investigations focusing on the evolution of OH* for different ignition systems.

In Figure 7 the results of a statistical analysis of all repetitions of above shown (Figure 6) image sequences for combustion with pure gasoline (compliant with DIN EN 228, RON = 95) are presented. On the bottom half of the diagram the mean values of detected OH* area of all measurement repetitions are presented over time. On the top half of the diagram the coefficient of variation (COV), which is standard deviation normalised by mean value, of the detected OH* area is shown. The calculation of COV is realised by the following formula (1):

$$\mathrm{COV}_{\mathrm{area}} = \frac{\sigma_{\mathrm{area}}}{\bar{x}_{\mathrm{area}}} \qquad \text{Eq. (1)}$$

For the CIS (red) an elevated signal of OH* is noted directly after ignition (1 ms, dashed line 'IGN'). This is followed by a slight decrease, presumably due to the fading plasma of the CIS at this stage. After that, however, subsequently there is a direct transition towards a steep increase in OH* area which marks the onset of flame-front propagation. With respect to the SPI (black), almost no signal of OH* is detected directly after ignition. Furthermore, it is only after a much longer pause that the steep increase of OH* signal, with an even steeper gradient than with the CIS, occurs. The time difference in occurrence of increasing OH* signal might be due to different rates and mechanisms of flame kernel development which has been published in several works already [28, 46, 47, 48].

As can be seen in the upper diagram, the fluctuations with CIS are comparatively high (< 60%) shortly after ignition whereas there is no such tendency with SPI. Subsequently, fluctuations with SPI are higher than with CIS and gradually

FIGURE 7 Area of detected OH* (bottom) and coefficient of variation of detected area (top) for both spark plug and corona ignition with conventional RON95-gasoline.

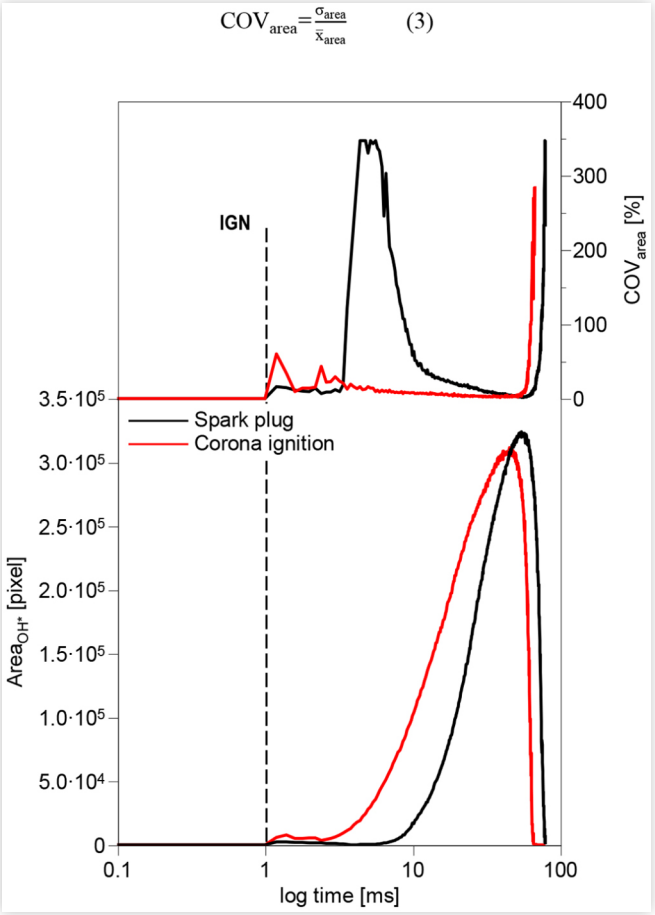

decrease until the point of maximum detected OH* area for both systems. Also, most prominently, there is a peak in fluctuations roughly 3 ms after ignition. This partly can be explained by the low levels of OH* at this point but COV levels only slowly decrease and are still elevated when spark induced flame-front propagation (high OH* levels) has started already. This behaviour is not found with CIS where COV levels remain low throughout flame-front propagation. Both systems feature a steep increase towards the end of the measurement which can be explained by the steep decrease in OH* signal at the end.

In Figure 8 dwell frequencies for both ignition systems are visualised by means of overlays of all measurements repetitions at a discrete time step. The pictures have been inverted for better visibility.

As can be seen at 1.8 ms, which corresponds to the COV peak for the CIS (cf. Figure 7), there are seemingly no variations to the residence of the OH* (black dot) around the spark-plug electrodes whereas small fluctuations thereof can be noted for the CIS (greyish areas). Afterwards, at 5.6 ms for the SPI, some measurement repetitions probably have not been

FIGURE 8 Dwell frequency for OH* area at discrete time steps.

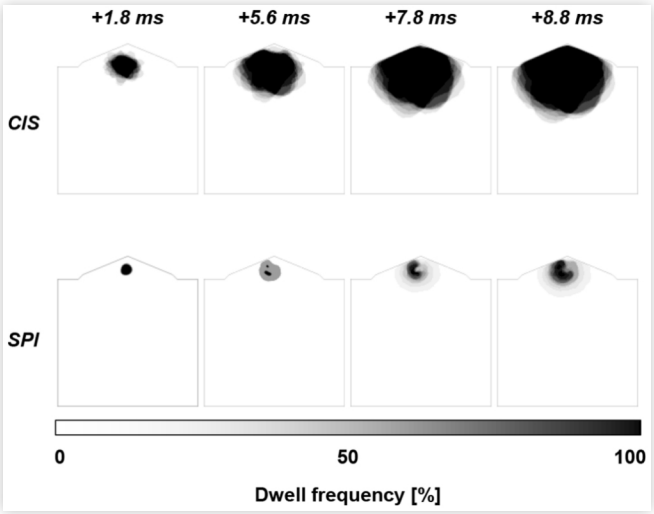

strong enough to be detected and therefore the grey overlay only represents <70% of all measurements. These delayed or omitted measurements influence flame-front propagation at later stages which can be noted in the overlays for later stages where OH* areas of varying sizes are seen as light-greyish circles around the darker common ground. For the CIS significantly denser black shapes are noted, which emphasise the superior stability of flame-front propagation for this system. The results showing the evolution of OH* area directly after ignition are in accordance with findings of Toedter et al. [29], who reported similar differences in OH* signal intensity directly after ignition for conventional spark-plug and corona ignition. The authors additionally found a decrease in OH* signal directly after ignition for the SPI. The same finding is evident for the results in this publication as can be noted in Figure 9.

FIGURE 9 Double-logarithmic depiction of detected OH* area for both ignition systems.

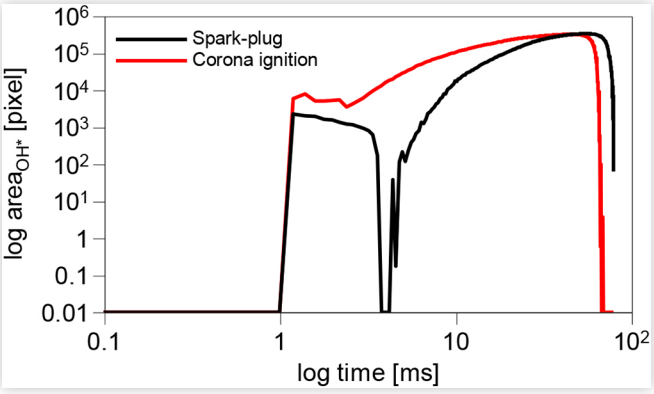

TABLE 3 OME1-blend overview.

Gasoline [Vol.-%]	OME1 [Vol.-%]	Abbreviation [-]
100	0	RON95
95	5	OME1-5
90	10	OME1-0
50	50	OME1-50

CIS and SPI with Gasoline and OME1-Blends

In the next series of experiments gasoline was blended with high-purity OME1. In terms of blending amount the step size resembles gasoline-ethanol blends commonly found in Central Europe such as E5 or E10 which represent 5 Vol.-% and 10 Vol.-% admixture of Ethanol, respectively. Additionally, as an extreme case, a 50 Vol.-% blend has been investigated as well (cf. Table 3).

The results thereof are presented in Figures 10 and 11 for CIS and SPI, respectively. As for the detected OH* area in Figure 10, the highest signal peak is found with pure gasoline followed by OME1-10, OME1-5 and OME1-50. Furthermore, the steep decrease in OH* signal towards the end is found

FIGURE 10 Area of detected OH* (bottom) and coefficient of variation of detected area (top) for corona ignition with conventional RON95-gasoline and 5, 10, 50 Vol.-% OME1-blends.

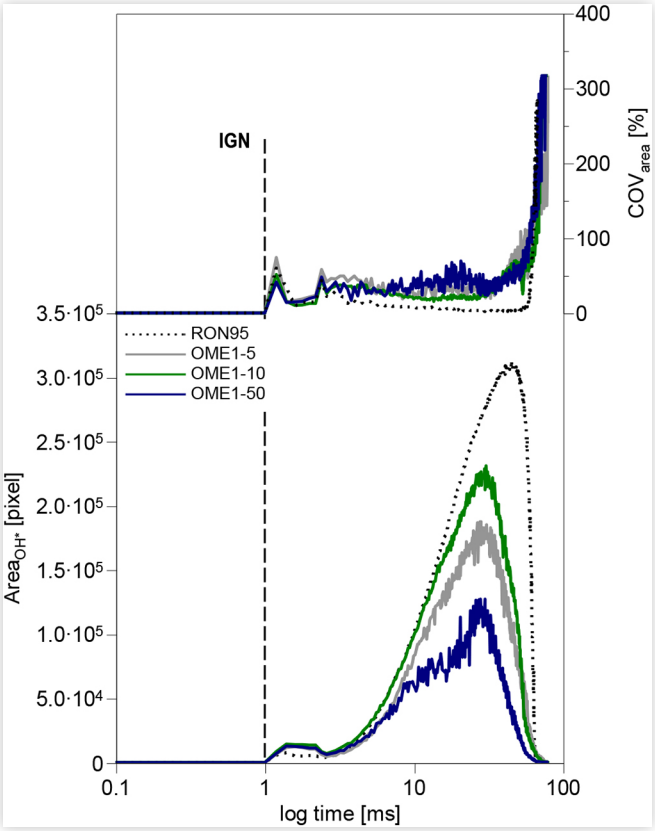

FIGURE 11 Area of detected OH* (bottom) and coefficient of variation of detected area (top) for spark-plug ignition with conventional RON95-gasoline and 5, 10, 50 Vol.-% OME1-blends.

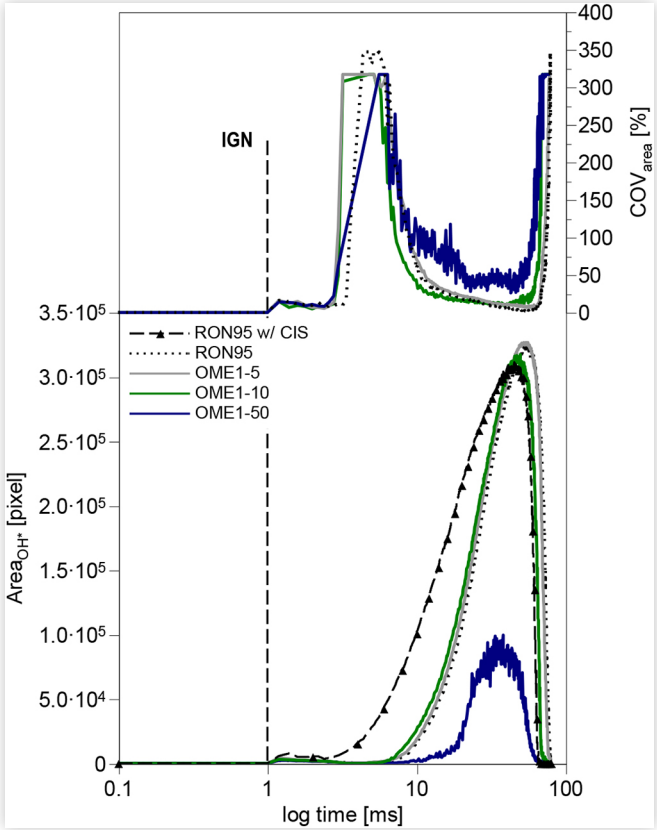

earlier for all blends than with pure gasoline. In terms of ignition, all blends exhibit an elevated signal in contrast to the 100% gasoline reference. The pixel count for OME1-10 at 1.8 ms for instance is over 2.5 times higher than that of the reference. Also, in between the three blends, the highest level is reached with OME1-10. Another aspect is the seemingly reduced gradient of OH* signal increase towards peak signal level. Here, as well, the gradient decreases in the same order as for the maximum signal. So, in between the blend steps there seems to be an optimum admixture with respect to OH* signal level during ignition and combustion.

To explain these phenomena three major effects have to be considered. The first aspect is the experimental premise to keep the equivalence ratio constant. When comparing the quotient of lower heating value for pure gasoline and pure OME1 with that for the stoichiometric ratios of both fuels (cf. Table 2) it becomes obvious, that OME1 features more than half (55%) the gravimetric lower heating value of gasoline. In contrast, the stoichiometric ratio of OME1 is just half (51%) that of gasoline. So by keeping the mixture's equivalence ratio constant roughly 4% more energy content have been introduced when comparing pure OME1 to pure gasoline. This discrepancy naturally closes towards lower admixtures, so the effect gets less distinct (OME1-50: 1.79%). Secondly, due

to OME1's high oxygen content, an increase in admixture of OME1 leads to an increased amount of fuel-bound oxygen in the mixture, which could increase formation of OH*. The equivalence ratio has been kept constant for all experiments and thus, thirdly, with OME1's low stoichiometric ratio and increased blending amount, an increased total fuel mass needs to be introduced at constant air mass.

For example, with reference to the fuel mass introduced for pure gasoline, an additional 38.4 wt.-% are introduced for OME1-50. The liquid fuel is injected and, by evaporating, cools down the combustion chamber. Despite pure OME1's low boiling temperature ($T_B = 42$ °C) and reduced heat of vaporisation (cf. Table 2) the blends' boiling curves are not significantly lowered in comparison to that of pure gasoline (cf. Figure 4). Furthermore this effect should be more pronounced at low temperature boundary conditions such as those applied in these experiments. So, due to the increased mass to be evaporated, overall process temperatures are reduced and combustion is slowed down. Another aspect is the way oxygen is supplied to the combustion. Whereas, in case of gasoline, the oxygen is supplied via the combustion air only, in case of OME1 it is partly supplied via the introduced air but also fuel-bound within the molecule. The strong influence of temperature on deflagratively propagating flames from homogeneous, spark ignited mixtures has been shown by Gu et al. [49]. By means of these hypotheses, the peak order in OH* signal can be explained by competing influences which either tend to strengthen or weaken radical formation.

This is very obvious in the difference between OME1-5 and OME1-10 where the influence of high oxygen content seems to be dominant whereas for OME1-50 the influence of fuel mass to evaporate seems to be stronger again. The same tendency, although weaker, can be seen during the time period of ignition. Regarding COV_{area} in Figure 10, reduced fluctuations of detected OH* area during the time period of ignition can be noted for all blends except OME1-5. Furthermore the peak of variation seems to be advanced and less pronounced, especially for the two highest admixtures of OME1. In contrast, an elevated level of fluctuations is evident after onset of flame front propagation with lowest levels for OME1-10. Hence, stability benefits during ignition do not seem to propagate towards subsequent flame front propagation. In Figure 11 the results of a variation of OME1 admixture for spark-plug ignition are presented.

With regard to the maximum OH* signal peak, there seems to be an even higher signal for OME1-5 than the gasoline reference. Contrary to the behaviour with CIS, a higher admixture of 10 Vol.-% results in a reduced peak. During the time period of ignition there are no visual differences whatsoever. With OME1-10 and, less pronounced, with OME1-5 the rise of OH* signal marking the onset of flame-front propagation takes place earlier than for the reference. This, as well, is different to what has been observed for CIS where no accelerated OH* signal rise could be noted. For OME1-50 the qualitative behaviour is similar for both ignition systems.

Apart from the effects already discussed for Figure 10, the time for mixture formation is an additional effect to be considered when comparing results of CIS and SPI. To illustrate the differing time intervals available for mixture formation the course of OH* signal for the gasoline reference with CIS (dashed black line, triangular markers) is plotted in Figure 11 as well. Hence, it may be assumed the air-fuel mixture for SPI is in a more homogeneous state. Therefore more heat has been deducted from the combustion chamber at the onset of flame-front propagation which strengthens the influence of fuel mass introduced to the combustion chamber. On the other side this weakens the influence of fuel-bound oxygen. The combination of both factors results in the order of maximum OH* peaks in Figure 11. With regard to COV_{area} in Figure 11 no significant differences are observed directly after ignition (1 ms). This also confirms that no significant alterations have taken place in the OH* signal level as discussed earlier. Afterwards, during the time period of flame-kernel development, reductions in peak levels of fluctuation can be noted for all blend steps compared to the gasoline reference. Consistent with an earlier onset of flame-front propagation, the phase of high fluctuations commences earlier for OME1-5 and OME1-10. The duration of this phase then is most reduced for OME1-10 while OME1-5 and the gasoline reference exhibit an almost identical course during steeply dropping fluctuations. Hence, with OME1-10 a reduction in peak-level and duration of the highly fluctuating phase of flame-kernel development is feasible. For OME1-5, apart from a reduction in peak-level the duration of this phase is increased. OME1-50, while not exhibiting throwbacks during ignition, suffers from highly fluctuating OH* area signals throughout flame-front propagation.

CIS with Gasoline and DMC-Blends

In this section the results for DMC-blended combustion are presented. Alas, due to high rates of 'misfires', it wasn't possible to realise reproducible combustion with spark-plug ignition. The authors attribute this to physical properties of DMC such as very low stoichiometric ratio whereby high fuel mass had to be injected. In case of DMC-50 over three times the fuel mass as for the reference had to be evaporated with increased heat of vaporization (cf. Table 2). The fuel-blend abbreviations are listed in Table 4.

In Figure 12 the results of a DMC admixture variation for CIS are presented. With regard to OH* signal peak a running order similar to that of the OME1 variation can be observed. However, courses for DMC-5 and DMC-10 are much closer than with OME1 admixture. Furthermore

TABLE 4 DMC-blend overview.

Gasoline [Vol.-%]	DMC [Vol.-%]	Abbreviation [-]
100	0	RON95
95	5	DMC-5
90	10	DMC-10
50	50	DMC-50

FIGURE 12 Area of detected OH* (bottom) and coefficient of variation of detected area (top) for corona ignition with conventional RON95-gasoline and 5, 10, 50 Vol.-% DMC-blends.

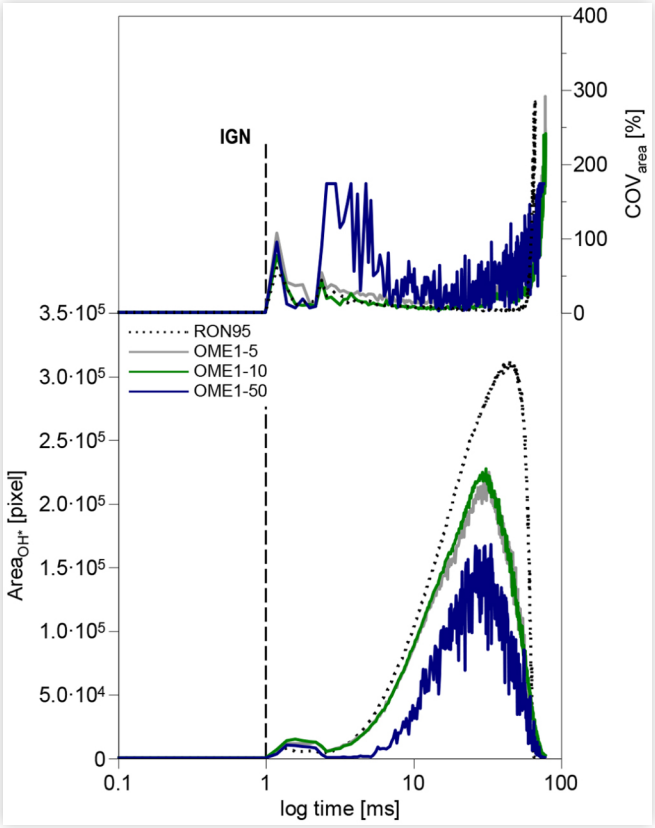

FIGURE 13 Measured RON for OME1 and DMC blend steps.

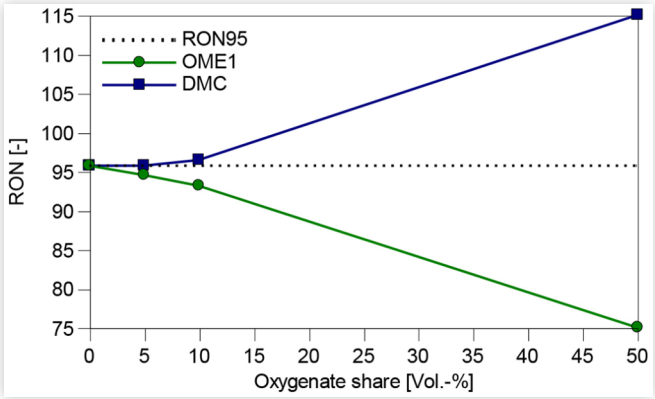

the rise towards OH* peak is delayed for 5, 10% and, much more, for 50% admixture of DMC. In contrast, the slope of OME1-10 is congruent to that of the reference and only 5 and 50% OME1 admixture show delayed OH* formation rates. As for the ignition there are elevated OH* levels for all blends but differences in between the blend steps are clearly discernible. The maximum OH* peak during ignition is reached with DMC-10. Interestingly, DMC-50 shows a drop in OH* signal after ignition seemingly similar to that of a spark-plug ignited mixture.

Considering OH* area fluctuations there is a shift of peak COV levels closer towards ignition timing as has been observed with OME1 admixture. Contrary to OME1-blends, though, fluctuations with all DMC admixtures exhibit similarly high COV levels as the gasoline reference. Fluctuations with DMC-50 are strongly increased throughout the whole measurement.

To explain the behavioural differences of OME1 and DMC admixtures different physical properties of both fuels have to be taken into account. Firstly, DMC has an even higher oxygen content (53.3 wt.-%) than OME1 (42.1 wt.-%) which results in a reduced stoichiometric ratio for DMC (4.58 kg/kg) compared to OME1 (7.23 kg/kg) (cf. Table 2). So, at constant air-mass within the CVCC, more fuel is introduced and has to be evaporated which in turn cools down the combustion chamber. Furthermore, DMC exhibits an increased heat of vaporisation with regard to RON95 or gasoline. In case of a 50% admixture, 13.9 wt.-% more DMC have to be introduced than OME1. This effect is somewhat attenuated by the high volumetric mass density of DMC (1007 kg/m^3). However, due to the high oxygen content, DMC has a very low energetic content as well (14.5 MJ/kg), so by keeping the equivalence ratio constant less fuel energy is introduced compared to the gasoline reference or OME1-blends.

Another aspect is the mixture's increasing knock-resistance with increasing DMC content whereas OME1 mixtures behave contrarily. To that end, results of RON measurements conducted on the blends in this publication are presented in Figure 13. While increased knock resistance is desirable in critical engine boundary conditions, in less critical conditions it reduces reactions rates by reduced ignitability.

CIS in Different Plasma Modes

In the final step two different ignition modes of the corona ignition are compared for RON95, OME1-10 and DMC-10. The two latter of which have been proven to be feasible blend candidates for application in an IC engine. Typically, due to an inhomogeneous electric field between the electrodes, the corona ignition system induces an NTP, i.e. a partial discharge, with several discharge streamers originating from the igniter's electrode tips whereby a large volume of the fuel-air mixture is affected. Boundary conditions in this publication, such as pressure, electrode gap [50] and ignition controller parameters, such as applied voltage and burst duration have been set below the electric arc limit, which marks the change in regime from partial discharge (cold plasma) towards arc discharge (hot plasma). Above the arc limit the system behaves similar to a spark-plug, i.e. the CIS produces big electric arcs subjecting the igniter electrodes to additional wear on account of high temperatures in the discharge channel. In Figure 14 combustion of DMC-10 initiated by NTP streamers (top row) and by a corona ignition in arc mode (bottom row) is presented.

FIGURE 14 Combustion of DMC-10 without arc (top row) and with arc (bottom row).

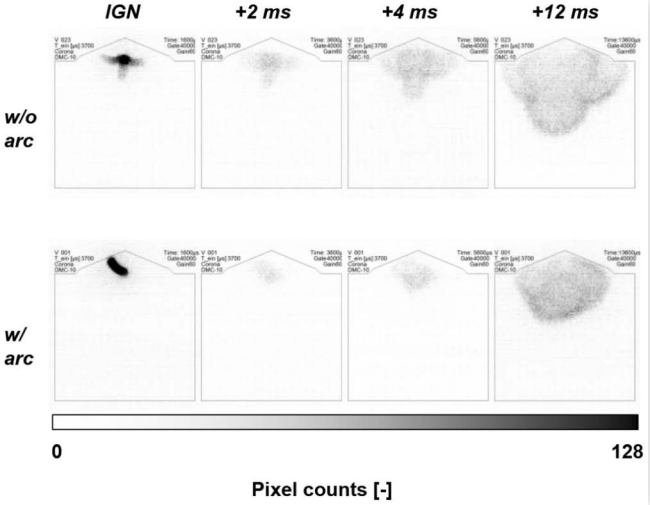

FIGURE 15 Area of detected OH* for various air ratios and corona ignition with 5, 10, 50 Vol.-% DMC-blends.

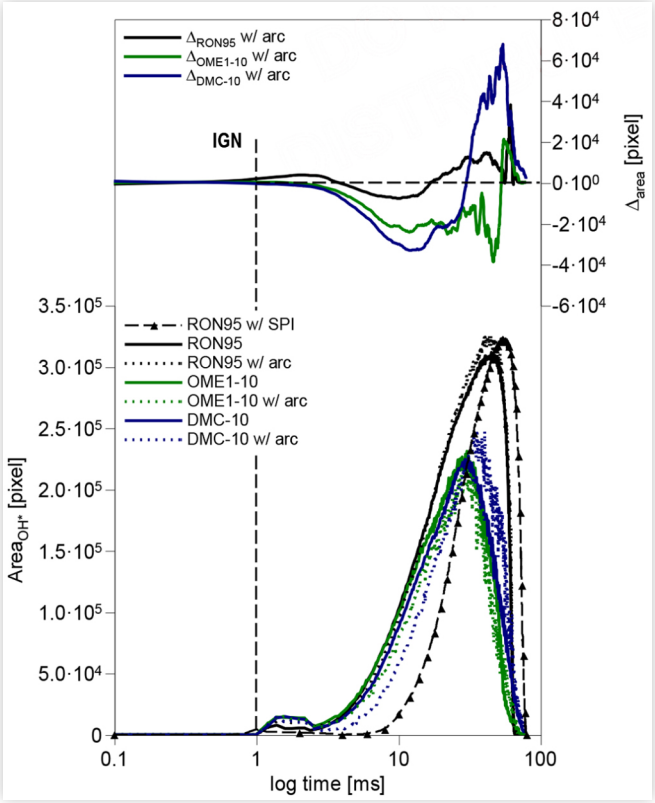

The pictures have been inverted for better visibility. During ignition an arc towards the chamber's pent-roof is clearly visible for combustion with arc. Furthermore the arc is quite bright (black) and the penetrated volume is reduced. However, in comparison with the arc-volume of a conventional SPI it is still large. In contrast, three visible streamers have formed for combustion without arc. During subsequent flame-front propagation, visible differences in the engulfed OH* area and the shape thereof are observed. In case of the combustion without arc the shape of the OH* area seems to have evolved from the position of the streamer discharges during ignition timing. This is not the case for combustion with arc where expansion and shape of the OH* area qualitatively mimick that of an ignition with a spark-plug (cf. Figure 6). So, especially when the corona ignition is operated near the arc-limit, fluctuations in flow field, gas density et cetera stochastically cause occurring arcs. To study sensitivity of the ignition and subsequent flame-front propagation towards an arcing CIS, both discharge modes are compared for operation with aforementioned three fuels. The results thereof are presented in Figure 15.

On the bottom half of the diagram the course of OH* area is presented for RON95 (black), OME1-10 (green) and DMC-10 (blue). Ignition by NTP plasma is marked in solid lines while ignition with an arc is marked by dashed lines for each fuel. As a reference, the course of OH* area for RON95 with spark-plug ignition is presented in black dashed line with triangular markers. On the top half of the diagram the difference in OH* area (Δ_{area}) between both ignition modes at each time step is presented. To enhance readability the data in the top diagram is filtered by Savitzky-Golay filtering [51].

For RON95 a slightly increased OH* level during ignition can be detected for arc-induced combustion. This can partly be attributed to the high brightness of the arc (cf. Figure 14). Whereas slightly reduced OH* levels can be noted during onset of flame-front propagation the peak level is increased (cf. top half of Figure 15). With OME1-10 OH* levels during ignition remain constant whereas after onset of flame-front propagation these are visibly reduced, i.e. OH* formation is retarded (green line, top half of Figure 15). Ultimately with DMC1-10 the OH* count during ignition is almost constant while subsequent OH* formation is even more retarded than with OME1-10 (blue line, top half of Figure 15). Afterwards the OH* peak is increased compared to the ignition without arcs. When comparing the slope with that of RON95 ignited by SPI, the corona ignition with arcs still exhibits a significant advantage in terms of OH* formation rate even with DMC-10. This can be attributed to the increased volume and length of the single arc in comparison to a small spark locally restricted to the area in between the spark plug electrodes (cf. Figures 6 and 14).

Subsuming, the following observations have been made: In terms of OH* formation, a corona ignition with arcs exhibits a reduction in the early stages of flame-front propagation with the magnitude thereof depending on the fuel. Yet, despite the same underlying physical principle of thermal plasma as a conventional spark-plug ignition, the CIS shows a visibly increased discharge volume and is not locally restricted. The sensitivity towards unwanted-for arcs is increasing in the order of RON95, OME1-10 and DMC-10 which also happens to be the order of increasing oxygen content and therefore fuel mass introduced. Consequently sensitivity is increased for more challenging ignition conditions and also indicates application areas, where deployment of a corona ignition system has additional potential.

Conclusions

From the results presented in this paper, the following conclusions can be drawn:

1. Swelling tests with all studied blends were conducted on various elastomer materials. OME1 as a blending component showed less adverse effects. Lowest swelling rates of <5% for all blend steps and regardless of the oxygenate could be noted for PER G75 LT (FFKM 72), which is a cost-effective perfluoroelastomer.
2. Optical high-speed measurements of OH* chemiluminescence with gasoline combustion ignited by either spark-plug or corona ignition have confirmed results of other publications where reduced burn delay and improved ignition stability with corona ignition were reported. High fluctuations of OH* signal (>340%) are evident with the spark-plug ignition. Stability with corona ignition shows quite contrary results with a highly stable (reproducible) course of OH* formation throughout all stages of the measurement.
3. Experiments with varying admixture of OME1 for both ignition systems have shown ambivalent results in OH* formation. A positive interaction between oxygenate-bound oxygen and ignition system could only be identified for the corona ignition. Reduced OH* formation peaks and gradients are found for all blends in spite of increased fuel and, consequently, oxygen mass within the combustion chamber It can be hypothesised a corona ignition will be able to deliver high OH* formation peaks if boundary conditions for mixture formation were improved. OH* formation fluctuations exhibit small benefits during ignition (CIS, SPI) but deteriorate throughout onset of OH* formation with the smallest drawbacks for OME1-10.
4. Experiments with varying admixture of DMC were limited to corona ignition. OH* formation towards peak level was retarded for all blends with the maximum peak for DMC-10. Fluctuations during ignition were increased for all DMC blends especially for DMC-50. The behavioural differences from OME1 to DMC can be explained by physical properties such as increased oxygen content (fuel mass), heat of vaporization and knock resistance as well as reduced energy content. Based on the experimental results DMC-10 is the most promising fuel-blend as a gasoline substitute.
5. Finally OH* formation for corona ignition with and without electric breakthrough (arc) was studied to quantify sensitivity towards a positive interaction of pre-selected oxygenates OME1-10 and DMC-10 with the non-thermal plasma. An electric arc had but a small influence on the OH* count during ignition. However, afterwards, OH* formation was significantly retarded depending on the fuel deployed. The strongest delay was evident for DMC-10 which also exhibits the highest oxygen content and fuel mass introduced. Nevertheless, despite an arc, the corona ignition still demonstrated faster OH* formation rates than a spark-plug ignition which can be attributed to the increased discharge volume and no locally restricted occurrence of the discharge channel.

Contact Information

Dipl.-Ing. Thorsten Langhorst
Institute of Internal Combustion Engines
Karlsruhe Institute of Technology (KIT)
Rintheimer Querallee 2
76131 Karlsruhe, Germany
Thorsten.Langhorst@kit.edu

Acknowledgements

This research work was conducted within the project 'Profilregion Mobilitätssysteme Karlsruhe' funded by the 'Ministerium für Wissenschaft, Forschung und Kunst und das Ministerium für Finanzen und Wirtschaft des Landes Baden-Württemberg'. The authors express their thanks to them and all the project partners involved. The authors would also like to thank the students Moritz Grüninger and Montassar Saidani for their enthusiasm, effort and research spirit.

Definitions/Abbreviations

CAS - Chemical Abstracts Service

CIS - Corona ignition system

CN - Cetane number

COV_{area} - Coefficient of variation of OH* area

DMC - Dimethyl carbonate

HNBR 70 - HNBR 70, hydrated nitrile butadiene rubber

LHV - Lower heating value [MJ/kg]

LT 170 - FKM 70, fluoroelastomer

MON - Motor octane number

Ne 471 - CR 70, chloroprene rubber

OME - Oxymethylenether ($CH_3(OCH_2)_nOCH_3$)

P 700 - NBR 70, nitrile butadiene rubber

PER G75 LT - FFKM 72, perfluoroelastomer

RON - Research octane number

Si 970, FL - FVMQ 70, fluorsilicone

SPI - Spark-plug ignition

T_B - Boiling temperature [°C]

T_M - Melting temperature [°C]

Vi 110, S - FKM 70, fluoroelastomer

Vi 840 - FKM 80, fluoroelastomer

$\Delta H_{vaporisation}$ - Heat of vaporisation [kJ/kg]

References

1. European Climate Foundation (ECF), "Roadmap 2050-A Practical Guide to a Prosperous, Low-Carbon Europe," Brussels, 2010.
2. Europäische Parlament und der Rat der Europäischen Union, Das, "Verordnung (EG) Nr. 443/2009 des Europäischen Parlaments und des Rates," Brussels, 2009.
3. Europäische Parlament und der Rat der Europäischen Union, Das, "Richtlinie 2009/28/EG des Europäischen Parlaments und des Rates," Brussels, 2009.
4. Searchinger, T. and Heimlich, R., "Avoiding Bioenergy Competition for Food Crops and Land," Creat. a Sustain. Food Futur. (9), 2015, 44.
5. Tessum, C.W., Hill, J.D., and Marshall, J.D., "Life Cycle Air Quality Impacts of Conventional and Alternative Light-Duty Transportation in the United States," *Proc. Natl. Acad. Sci. U.S.A.* 111(52):18490-18495, 2014, doi:10.1073/pnas.1406853111.
6. Lee, K., Seong, H., Sakai, S., Hageman, M. et al., "Detailed Morphological Properties of Nanoparticles from Gasoline Direct Injection Engine Combustion of Ethanol Blends," SAE Technical Paper 2013-24-0185, 2013, doi:10.4271/2013-24-0185.
7. Lee, K., Seong, H., Church, W., and McConnell, S., "Examination of Particulate Emissions from Alcohol Blended Fuel Combustion in a Gasoline Direct Injection Engine," in *Eighth Int. Conf. Model. Diagnostics Adv. Engine Syst. (COMODIA 2012)*, Fukuoka, Japan, 305-310, 2012.
8. Wang-Hansen, C., Ericsson, P., Lundberg, B., Skoglundh, M. et al., "Characterization of Particulate Matter from Direct Injected Gasoline Engines," *Top. Catal.* 56(1-8):446-451, 2013, doi:10.1007/s11244-013-9994-4.
9. Luo, Y., Zhu, L., Fang, J., Zhuang, Z. et al., "Size Distribution, Chemical Composition and Oxidation Reactivity of Particulate Matter from Gasoline Direct Injection (GDI) Engine Fueled with Ethanol-Gasoline Fuel," *Appl. Therm. Eng.* 89:647-655, 2015, doi:10.1016/j.applthermaleng.2015.06.060.
10. Storch, M., Hinrichsen, F., Wensing, M., Will, S. et al., "The Effect of Ethanol Blending on Mixture Formation, Combustion and Soot Emission Studied in an Optical DISI Engine," *Appl. Energy* 156:783-792, 2015, doi:10.1016/j.apenergy.2015.06.030.
11. Sauer, J., Kolb, T., and Günther, A., "BtL - Das Karlsruher Bioliq-Verfahren," *Chemie Ing. Tech.* 86(9):1356-1356, 2014, doi:10.1002/cite.201450348.
12. Lautenschütz, L., "Neue Erkenntnisse in der Syntheseoptimierung oligomerer Oxymethylendimethylether aus Dimethoxymethan und Trioxan," Dissertation, Karlsruhe Institute of Technology (KIT), Karlsruhe, 2015.
13. Lautenschütz, L., Oestreich, D., Seidenspinner, P., Arnold, U. et al., "Physico-Chemical Properties and Fuel Characteristics of Oxymethylene Dialkyl Ethers," *Fuel* 173:129-137, 2016, doi:10.1016/j.fuel.2016.01.060.
14. Jacob, E. and Maus, W., "Oxymethylene Ether as Potentially Carbon-Neutral Fuel for Clean Diesel Engines Part 2: Compliance with the Sustainability Requirement," *MTZ Worldw.* 78(3):52-57, 2017, doi:10.1007/s38313-017-0002-4.
15. Feiling, A., Münz, M., and Beidl, C., "Potenzial des Synthetischen Kraftstoffs OME 1b," *Mot. Zeitschrift* 2016:16-21, 2016.
16. Iannuzzi, S., Barro, C., Boulouchos, K., and Burger, J., "Combustion Behavior and Soot Formation/Oxidation of Oxygenated Fuels in a Cylindrical Constant Volume Chamber," *Fuel* 167:49-59, 2016, doi:10.1016/j.fuel.2015.11.060.
17. Härtl, M., Seidenspinner, P., Jacob, E., and Wachtmeister, G., "Oxygenate Screening on a Heavy-Duty Diesel Engine and Emission Characteristics of Highly Oxygenated Oxymethylene Ether Fuel OME 1," *Fuel* 153:328-335, 2015, doi:10.1016/j.fuel.2015.03.012.
18. Bockhorn, H., *Soot Formation in Combustion*, (Berlin, Heidelberg: Springer-Verlag, 1994), ISBN: 3-540-58398-X.
19. Europäische Komission, "International Chemical Safety Card on Dimethyl Carbonate (616-38-6)," Int. Progr. Chem. Saf., 2005.
20. Europäische Parlament und der Rat der Europäischen Union, Das, "Verordnung (EG) Nr. 715/2007 Des Europäischen Parlaments und des Rates," Brussels, 2007.
21. Die Kommission der Europäischen Gemeinschaften, "Verordnung (EG) Nr. 692/2008 der Kommission," Brussels, 2008.
22. Die Europäische Kommission, "Verordnung (EU) 2016/646 der Kommission," Brussels, 2016.
23. Auerbach, B., "Eberspächer startet Serienproduktion von Ottopartikelfiltern," Springer Professional, 2017.
24. Schenk, M., Feßler, M., Rottengruber, H., and Fischer, H., "Comparison of the Thermodynamic Potential of Alternative Ignition Systems for SI-Engines," in *10th International Symposium on Combustion Diagnostics*, Baden-Baden, 138-157, May 22-23, 2012.
25. Berndt, F., "Ottomotorische Magerbrennverfahren: NOx- und partikelarme Verbrennung durch neue Zünd- und Einspritzkonzepte," Dissertation, TU Braunschweig, Braunschweig, ISBN: 9783844038446, 2015.
26. Wolf, T., Schenk, M., Schröter, M., Zellinger, F. et al., "RF-Corona-Ignition vs. Spark Ignition: A Comparison for Varying Thermodynamic Conditions and Combustion Strategies of Modern Turbocharged Gasoline Engines," *2nd International Conference on Ignition Systems for Gasoline Engines*, Berlin, Germany, 503-532, Nov 24-25, 2014.
27. Hampe, C., "Hochfrequenz-Zündung für ottomotorische Brennverfahren," Dissertation, Karlsruhe Institute of Technology, Karlsruhe, ISBN: 978-3-8325-4416-4, 2016.
28. Auzas, F., "Décharge radiofréquence produite dans les gaz à pression élevée pour le déclenchement de combustion," Dissertation, Université Paris Sud, Orsay, 2008.
29. Toedter, O., Heinz, A., Disch, C., Koch, T. et al., "Comparing Visualization of Inflammation at Transient Load Steps Comparing Ignition Systems," in Günther, M. and Sens, M., eds., *Ignition Systems for Gasoline Engines-3rd International Conference*, (Switzerland: Springer International Publishing, 2016), ISBN: 9783319455037, 325.
30. Ranji-Burachaloo, H., Masoomi-Godarzi, S., Khodadadi, A.A., and Mortazavi, Y., "Synergetic Effects of Plasma and Metal Oxide Catalysts on Diesel Soot Oxidation," *Appl. Catal. B Environ.* 182:74-84, 2016, doi:10.1016/j.apcatb.2015.09.019.
31. Wang, P., Gu, W., Lei, L., Cai, Y., and Li, Z., "Micro-Structural and Components Evolution Mechanism of Particular Matter from Diesel Engines with Non-Thermal Plasma Technology," *Appl. Therm. Eng.* 91:1-10, 2015, doi:10.1016/j.applthermaleng.2015.08.010.

32. Storch, M., Nguyen, A.D., Wensing, M., Will, S., and Zigan, L., "Simultaneous High-Speed Imaging and Laser-Induced Incandescence (LII) for Investigation of the Sooting Combustion of Ethanol Fuel Blends in a DISI Engine," in *Proceedings of the European Combustion Meeting 2015*, Budapest, Hungary, Mar 30-Apr 2, 2015, doi:10.4271/2014-01-2617.
33. Burrows, J., Mixell, K., Reinicke, P.-B., Riess, M., and Sens, M., "Corona Ignition - Assessment of Physical Effects by Pressure Chamber, Rapid Compression Machine, and Single Cylinder Engine Testing," in *Ignition Systems for Gasoline Engines - 2nd International Conference*, Berlin, Germany, ISBN 9783944976228, 87-107, 2014.
34. Haber, L.C. and Vandsburger, U., "A Global Reaction Model for OH* Chemiluminescence Applied to a Laminar Flat-Flame Burner," *Combust. Sci. Technol.* 175(10):1859-1891, 2003, doi:10.1080/713713115.
35. Tinaut, F.V., Reyes, M., Giménez, B., and Pastor, J.V., "Measurements of OH* and CH* Chemiluminescence in Premixed Flames in a Constant Volume Combustion Bomb under Autoignition Conditions," *Energy and Fuels* 25(1):119-129, 2011, doi:10.1021/ef1013456.
36. Werler, M., "Untersuchungen der Niedertemperaturoxidation von Kohlenwasserstoffen in einer schnellen Kompressions-Expansions-Maschine," Dissertation, Karlsruhe Institute of Technology, Karlsruhe, 2016.
37. Maly, R. and Vogel, M., "Initiation and Propagation of Flame Fronts in Lean CH_4-Air Mixtures by the Three Modes of the Ignition Spark," *Symposium on Combustion* 17(1):821-831, 1979, doi:10.1016/S0082-0784(79)80079-X.
38. Pischinger, S., *Verbrennungsmotoren Band I*," 26th Edition, (Aachen: RWTH Aachen, 2007).
39. U.S. Coast Guard Department of Transportation, *CHRIS - Hazardous Chemical Data. Volume II*, 5th Edition, (Washington, DC: U.S. Government Printing Office, 1984).
40. Daubert, T.E. and Danner, R.P., *Physical and Thermodynamic Properties of Pure Chemicals Data Compilation* (Washington, DC, Taylor & Francis, 1989), ISBN: 9780891169482.
41. Deutsch, D., Oestreich, D., Lautenschütz, L., Haltenort, P. et al., "High Purity Oligomeric Oxymethylene Ethers as Diesel Fuels," *Chem. Ing. Tech.* 89(4):486-489, 2017, doi:10.1002/cite.201600158.
42. Sivanathan, S. and Chandran, H., "Investigation on the Performance and Emission Characteristics of Biodiesel and Its Blends with Oxygenated Additives in a Diesel Engine," SAE Technical Paper 2014-01-1261, 2014, doi:10.4271/2014-01-1261.
43. Lide, D.R., *CRC Handbook of Chemistry and Physics*, Internet Version, (London: Taylor & Francis, 2005), ISBN: 1482260964.
44. Otsu, N., "A Threshold Selection Method from Gray-Level Histograms," *IEEE Trans. Syst. Man. Cybern.* 9(1):62-66, 1979, doi:10.1109/TSMC.1979.4310076.
45. Pischinger, F., Adomeit, G., Krause, E., Pitt, R. et al., "Sonderforschungsbereich 224 'Motorische Verbrennung'," *Lehrstuhl Für Verbrennungskraftmaschinen* 729, 1995, http://www.sfb224.rwth-aachen.de/bericht.htm.
46. Kratzsch, M. and Günther, M., *Advanced Ignition Systems for Gasoline Engines*, (Renningen, Germany: Expert Verlag, 2013), ISBN: 9783816931904.
47. Shiraishi, T. and Urushihara, T., "Fundamental Analysis of Combustion Initiation Characteristics of Low Temperature Plasma Ignition for Internal Combustion Gasoline Engine," SAE Technical Paper 2011-01-0660, 2011, doi:10.4271/2011-01-0660.
48. Kosarev, I.N., Aleksandrov, N.L., Kindysheva, S.V., Starikovskaia, S.M. et al., "Kinetics of Ignition of Saturated Hydrocarbons by Nonequilibrium Plasma: C_2H_6- to C_5H_{12}-Containing Mixtures," *Combust. Flame* 156(1):221-233, 2009, doi:10.1016/j.combustflame.2008.07.013.
49. Gu, X.J., Emerson, D.R., and Bradley, D., "Modes of Reaction Front Propagation from Hot Spots," *Combust. Flame* 133(1-2):63-74, 2003, doi:10.1016/S0010-2180(02)00541-2.
50. Paschen, F., "Ueber die zum Funkenübergang in Luft, Wasserstoff und Kohlensäure bei verschiedenen Drucken erforderliche Potentialdifferenz," *Ann. Phys.* 273(5):69-96, 1889, doi:10.1002/andp.18892730505.
51. Savitzky, A. and Golay, M.J.E., "Smoothing and Differentiation of Data by Simplified Least Squares Procedures," *Anal. Chem.* 36(8):1627-1639, 1964, doi:10.1021/ac60214a047.
52. Härtl, M., Seidenspinner, P., Wachtmeister, G., and Jacob, E., "Synthetic Diesel Fuel OME1 a Pathway Out of the Soot-NOx Trade-Off," *MTZ Worldw.* 75(7-8):48-53, 2014, doi:10.1007/s38313-014-0173-1.
53. Härtl, M., Gaukel, K., Pélerin, D., and Wachtmeister, G., "Oxymethylene Ether as Potentially CO_2-Neutral Fuel for Clean Diesel Engines Part 1: Engine Testing," *MTZ Worldw.* 78(2):52-59, 2017, doi:10.1007/s38313-016-0163-6.
54. Kolah, A.K., Mahajani, S.M., and Sharma, M.M., "Acetalization of Formaldehyde with Methanol in Batch and Continuous Reactive Distillation Columns," *Ind. Eng. Chem. Res.* 35(10):3707-3720, 1996, doi:10.1021/ie950563x.
55. Masamoto, J. and Matsuzaki, K., "Development of Methylal Synthesis by Reactive Distillation," *J. Chem. Eng. Jpn.* 27(1):1-5, 1994, doi:10.1252/jcej.27.1.
56. Zhang, X., Zhang, S., and Jian, C., "Synthesis of Methylal by Catalytic Distillation," *Chem. Eng. Res. Des.* 89(6):573-580, 2011, doi:10.1016/j.cherd.2010.09.002.
57. Agirre, I., Barrio, V.L., Güemez, M.B., Cambra, J.F. et al., "Acetals as Possible Diesel Additives," in Santos Bernardes, M.A.D., ed., *Economic Effects of Biofuel Production*, (InTech, 2011), 299-316, ISBN: 978-953-307-178-7, doi:10.5772/697.
58. Matzner, M., Kurkjy, R.P., and Cotter, R.J., "The Chemistry of Chloroformates," *Chem. Rev.* 64(6):645-687, 1964, doi:10.1021/cr60232a004.
59. Babad, H. and Zeiler, A.G., "Chemistry of Phosgene," *Chem. Rev.* 73(1):75-91, 1973, doi:10.1021/cr60281a005.
60. Nishimura, K., Uchiumi, S., Fujii, K., Nishihara, K. et al., "*Process for Preparing a Diester of Oxalic Acid*," (United States, 1980), U.S. Patent US4,229,589A.
61. Miyazaki, Y., Shiomi, Y., Fujitsu, S., and Masunaga, K., "Process for the Preparation of Oxalic Acid Diesters," U.S. Patent 4,384,133 A, 1983.
62. Romano, U., Tesei, R., Cipriani, G., and Micucci, L., "Method for the Preparation of Esters of Carbonic Acid," U.S. Patent 4,218,391 A, 1980.
63. Hagen, G.P. and Spangler, M.J., "Continuous Catalytic Process for Preparation of Organic Carbonates," BP Amoco Corporation, U.S. Patent 5,750,759 A, 2000.

Appendix

Fuel Production Methodology

Sustainable production of both OME1 and DMC is possible by using methanol (MeOH) as raw material. MeOH can easily be produced from synthesis gas ($CO + H_2$), which in turn is obtained by gasification of waste biomass or water-gas-shift reaction of electrolytic H_2 and CO_2. Thereby, there is no conflict with the food chain by the consumption of forage crops for the production of 2nd generation biofuels. Oxymethylene ethers (OME_n, $CH_3(OCH_2)_nOCH_3$) can be used as diesel fuels. These oligomeric compounds show advantageous combustion properties and contribute to the solution of the soot-NO_x trade-off [14, 52, 53]. The addition of OMEs to gasoline has not been investigated yet. Due to its good availability, OME1 could be an interesting gasoline blend component. The direct synthesis of OME1 from MeOH is possible. However, the methods are not yet applied on industrial scale. The acid-catalyzed acetalization from aqueous methanolic formalin solution is the state of the art process to synthesize OME1, using acidic cation exchangers as catalysts [54, 55]. The equilibrium reaction of the synthesis is shown in Equation A.1:

$$2MeOH + CH_2O_{(aq)} \overset{H^+}{\rightleftharpoons} OME1 + H_2O \quad \text{Eq. (A.1)}$$

In large-scale processes, OME1 is continuously removed by catalytic reactive distillation, resulting in a high conversion of 99.8% at a reaction temperature of 90 °C [56, 57]. The process is technically feasible as the energy and investment costs are low and the product yield is high. On the other hand, production processes for DMC still need to be improved. Three processes have been applied in the industrial scale, whereof the phosgenation route [58, 59] has been abandoned some time ago and the UBE process [60, 61] does not use regeneratively producible educts. Only the ENIChem process [62] can provide a sustainable DMC production. The process is based on the oxidative carbonylation of methanol over a CuCl catalyst system, as shown in Equation A.2:

$$2MeOH + CO + 1/2O_2 \rightarrow DMC + H_2O \quad \text{Eq. (A.2)}$$

H_2O inhibits the activity and lowers the DMC selectivity of the catalyst. To counter this effect, DME can be added to the educt feed, whereby H_2O is consumed due to the formation of methanol by hydrolysis of DME. In a $MeOH/DME/CO/O_2$ educt feed, DMC and OME1 can be formed parallel as main products, with a selectivity of 50%, respectively since MeOH is converted into formalin in a secondary reaction and reacts further to OME1, as shown in Equation A.1 [63].

Swelling Behaviour of Gasoline-Oxygenate Blends

In order to test the compatibility of the gasoline-oxygenate blends with the sealing materials in the test-rig, the swelling behaviour of several elastomer sealing rings (purchased by COG, Germany), after being exposed to the blends, was investigated. To perform the measurements, the test rings were put in screw cap glasses filled with the blends, well-sealed and stored at 28 °C. The following procedures were performed before, after 24 h and after 48 h exposure:

1. The inner diameter was measured with a digital caliper with two decimal places. The measuring jaws have been set in a way that the ring just falls down from the caliper. The measurement was carried out 5 times for each ring, with the ring being rotated further before each measurement. The arithmetic average of the measured values was calculated, as well as the standard deviation.
2. The thickness of the rings was measured with a digital caliper, analogous to the inner diameter.
3. The weight of the rings was measured with a scale (0.1 mg).
4. The rings were photographed with a camera on a fixed stand with millimeter paper as scale.

The arithmetic average of all measured values for each blend was calculated and the results were classified in the following categories:

A = 0-5% swelling of the elastomer.

B = 5-10% swelling of the elastomer.

C = 10-20% swelling of the elastomer.

D = more than 20% swelling of the elastomer.

The swelling behaviour of all tested elastomer sealing rings after 48 h exposure to the gasoline-oxygenate blends is shown in Tables A.1 and A.2.

As can be seen best results for all OME1-blends in terms of low swelling can be achieved with Vi 840 or PER G75 LT, which is also referred to as FFKM 72, a cost-efficient perfluoroelastomer. Alternative designations for the elastomers in both tables are given in the Definitions/Abbreviations list.

Swelling experiments with all DMC-blends yielded same results as to the most suitable sealing elastomer. Here as well PER G75 LT showed smallest swellings for all blends. Comparing negative effects of admixtures of both oxygenates, DMC seems to have a worse impact on swelling, especially for HNBR 70 and P 700. Naturally there is a trend of increased swelling for increased admixture regardless of the oxygenate.

TABLE A.1 Swelling behaviour of the sealing rings in gasoline-OME1 blends after 48 h exposure.

Material	5 Vol.-% OME1	10 Vol.-% OME1	50 Vol.-% OME1
HNBR 70	C	C	C
P 700	C	C	C
Ne 471	B	C	B
LT 170	A	B	B
Vi 110,S	B	B	C
Si 970, FL	B	B	A
Vi 840	A	B	B
PER G75 LT	A	A	A

TABLE A.2 Swelling behaviour of the sealing rings in gasoline-DMC blends after 48 h exposure.

Material	5 Vol.-% DMC	10 Vol.-% DMC	50 Vol.-% DMC
HNBR 70	C	C	D
P 700	C	C	D
Ne 471	B	B	C
LT 170	A	B	C
Vi 110, S	B	C	D
Si 970, FL	B	B	C
Vi 840	B	B	C
PER G75 LT	A	A	A